infrastructures

MDPI

Article

Analysis of Condensation Phenomena in a Long Subsea Road Tunnel in Korea and Development of the Condensation Prediction Diagram

Hyogyu Kim [1] and Chang-Woo Lee [2,*]

[1] Jusung G&B Inc., Guri 11901, Republic of Korea; hgkim@gnbeng.com
[2] Department of Energy and Mineral Resources Eng, Dong-A University, Busan 49315, Republic of Korea
* Correspondence: cwlee@dau.ac.kr

Abstract

Road tunnel ventilation systems have traditionally been designed to dilute vehicle-generated pollutants and control smoke during fires. However, the thermal environment, including temperature and humidity, is not the variable taken into consideration. Despite the operation of its ventilation system, Boryeong Subsea Tunnel (6.9 km), the longest subsea road tunnel in Korea, has experienced severe condensation since its opening in December 2021. As hot, humid ambient air enters the tunnel and meets wall surfaces cooled by seawater and the surrounding ground, condensation and fog may form, reducing visibility. To investigate the causes of condensation and develop a decision-making tool for prediction, a variety of tasks were carried out: (1) field measurements of temperature, humidity, tunnel wall temperature, and tunnel air velocity; (2) development of a 1D model for condensation rate quantification; and (3) 3D CFD simulations. Condensation occurred mainly from June to September, with the most severe conditions in July and August. Both the 1D model analysis and the CFD simulations showed good agreement with field measurement data, with wall temperature errors within 7.3%. Under current traffic conditions (with a peak of approximately 250 veh/h), the annual condensation volume was estimated at approximately 12,415 ton/year. Under the design traffic volume (1550 veh/h), heat from vehicles was found to effectively suppress condensation. The Condensation Contour Map (CCM) was developed as a decision support tool to predict the likelihood and amount of condensation based on the tunnel air temperature and humidity conditions. The results of this study clearly indicate that condensation should be explicitly considered in the design and operation of long subsea road tunnels.

Keywords: subsea tunnel; condensation; dew point temperature; moist air analysis; CFD simulation; field measurement; Boryeong tunnel; ventilation; Condensation Contour Map (CCM)

Check for updates

Academic Editor: Xiaodong Song

Received: 21 May 2026
Revised: 16 June 2026
Accepted: 18 June 2026
Published: 19 June 2026

1. Introduction

Ventilation and fire safety systems in road tunnels have traditionally been designed to dilute or remove pollutants (CO, NOx, particulate matter, etc.) emitted by vehicles and to control smoke in the event of a fire. In general, road tunnels are therefore designed with a primary focus on air quality and fire safety rather than on thermal environment control [1,2]. These design assumptions are reasonable for conventional mountain and urban tunnels, where humidity-related operational problems are usually secondary. However, the construction and operation of subsea tunnels present fundamentally different environmental challenges. While ground temperature remains relatively stable in mountain tunnels, subsea tunnels pass beneath the sea where water temperature varies seasonally, resulting in different tunnel wall temperature conditions. More importantly, influenced by a maritime climate, hot, humid air enters the subsea tunnel, particularly during summer. When this hot, humid ambient air comes into contact with the tunnel walls cooled by the seawater and surrounding ground, the water vapor in the airflow becomes saturated, and, depending on the thermal environment, condensation can be observed.

Condensation in subsea tunnels is not a problem unique to the Boryeong Subsea Tunnel, as similar phenomena have been reported in major long subsea tunnels worldwide. In the Channel Tunnel (50.5 km), high humidity and condensation have been recognized as persistent operational challenges since its opening. Bradbury et al. (1997) reported problems in the Channel Tunnel such as equipment corrosion, electrical insulation failure, and reduced visibility due to internal humidity and condensation [3]. They analyzed the physical mechanisms of moisture transport and enthalpy changes, and discussed humidity control strategies. This study demonstrated that condensation in long subsea tunnels can directly affect equipment reliability and safety beyond mere environmental discomfort.

The Seikan Tunnel in Japan (53.85 km, with a 23.3 km subsea section), the longest railroad tunnel in the world, reportedly maintains an internal temperature of approximately 20 °C year-round, with a relative humidity of 80–90% [4]. This high-humidity environment causes condensation problems on train car bodies. During the design of the Hokkaido Shinkansen H5-series vehicles, which entered service in 2016, condensation, snow accretion, and icing were identified as three key design challenges [5]. The condensation issues in the Seikan Tunnel clearly illustrate the impact of the constant high-humidity environment in subsea tunnels on vehicles and equipment.

Norway possesses the world's largest number of subsea road tunnels (approximately 40) and has the most extensive operational experiences. In the Nordkapp Subsea Tunnel (6.8 km, with a maximum depth of 212 m below sea level), fog formation has been reported near the lowest point [6], attributed to condensation phenomena resulting from thermal interaction between the cold walls in the deepest section and the moist air within the tunnel. The Ryfast Tunnel (14.4 km, maximum depth 292 m), currently the world's longest and deepest subsea road tunnel, also faces similar humidity management challenges. Even more severe condensation conditions are anticipated in the Rogfast Tunnel (26.7 km, with a maximum depth of 392 m), which is scheduled to open in 2033 [7]. Lervåg (2005) of SINTEF investigated factors affecting condensation formation in Norwegian subsea tunnels [8], indicating that condensation phenomena are common problems prevalent in Northern European regions.

In China, condensation phenomena in railroad tunnels in hot, humid regions have been systematically studied. Yan et al. (2017) conducted field measurements of tunnel wall temperature, air temperature, and relative humidity distributions in eight railroad tunnels and performed fluid–solid coupled numerical analysis using ABAQUS [9]. Their results showed that the temperature and humidity distributions in long tunnels can be divided into three zones: a quick-change region, a smooth transitional region, and a constant region, with wall condensation in hot, humid areas primarily caused by the temperature difference between the inside and outside of the tunnel, along with high humidity.

Under the research program of the Swiss Federal Roads Office (ASTRA), Bopp and Peter (2006) systematically investigated windshield fogging phenomena in road tunnels [10]. They conducted surveys, theoretical studies, model calculations, and field measurements in three problematic tunnels, revealing that windshield fogging can pose serious safety risks in bidirectional tunnels longer than 1400 m. They proposed an excess moisture content of 1.5 g/m^3 as the critical threshold for fogging onset and reported that dew point control through intermediate exhaust ventilation systems is an effective mitigation measure. This study demonstrated that condensation phenomena in road tunnels constitute a serious issue directly affecting driving safety, extending beyond structural concerns.

Yang et al. (2022) conducted a comprehensive review of ventilation and environmental control in underground spaces [11], identifying condensation as a major cause of equipment deterioration and reduced operational efficiency in underground structures.

Research on condensation in utility tunnels has been relatively active. Park et al. (2022) utilized CFD for air conditioning system design to reduce condensation in underground utility tunnels, reporting through field experiments that condensation occurs at relative humidity levels above 95% during summer [12]. Tai et al. (2020) conducted field measurements of temperature and humidity and analyzed condensation phenomena inside utility tunnels [13], while You et al. (2017) studied condensation on building interior surfaces in high-humidity environments [14]. Ryu et al. (2017) [15], Seong et al. (2018) [16], and Yoon et al. (2014) [17] conducted studies on thermal characteristics, temperature/humidity distributions, and condensation identification in underground utility tunnels in Korea. While these studies provide useful insights into condensation mechanisms in enclosed or semi-enclosed underground structures, the environmental conditions differ from those in road tunnels, where traffic-induced ventilation and vehicle heat generation are present.

Regarding fundamental research on tunnel thermal environments, Peavy (1961) performed a theoretical analysis of heating and cooling of air flowing through underground tunnels [18], and Li et al. (2015) reported long-term continuous monitoring results of tunnel lining surface temperature in cold regions [19]. Liu et al. (2004) conducted CFD prediction and experimental validation of condensation on wall surfaces, confirming the feasibility of predicting condensation phenomena through CFD [20]. As fundamental theoretical studies on evaporation and condensation, Jodat (2012) [21] and Aldarabseh (2020) [22] investigated water evaporation rate prediction under various convective conditions and free water surface evaporation rates, respectively. Kim (2022) [23] published a basic study of the causes of road tunnel condensation and possible countermeasures.

Generally, the findings mentioned above show that condensation in subsea tunnels is a recurring operational challenge in major tunnels worldwide. However, most of the existing relevant studies have mainly focused on (a) qualitative observations in railroad tunnels, (b) CFD-based analyses in utility tunnels, and (c) windshield fogging in road tunnels. There is a lack of comprehensive research on long subsea road tunnels, integrating field measurements, theoretical quantitative analysis, and three-dimensional CFD simulation.

This study aims to analyze the severe condensation issues experienced in the Boryeong Subsea Tunnel (6.9 km), Korea's longest subsea tunnel, and to develop an engineering tool for condensation prediction. The ultimate goal is to eliminate the condensation problem and to optimize the design and operation of long subsea tunnels anticipated for future construction in similar environments.

This study applies three approaches to analyze the condensation phenomena in the Boryeong Subsea Tunnel: (1) field measurements to characterize the thermal environment inside and outside the tunnel, together with wall temperature changes; (2) development of a 1D model for condensation rate quantification along the tunnel axis, taking into account moist air thermodynamics, heat transfer through the tunnel wall, vehicle heat generation, exhaust water vapor emissions, and wall surface evaporation; and (3) 3D CFD simulations to evaluate the 1D model and resolve detailed spatial distributions. Based on these results, the Condensation Contour Map (CCM) was developed as a practical condensation rate prediction tool.

https://doi.org/10.3390/infrastructures11060209

2. Tunnel Overview

2.1. Tunnel Specifications and Ventilation System

The Boryeong Subsea Tunnel consists of twin two-lane tunnels with lengths of 6916 m (Boryeong-bound) and 6927 m (Taean-bound). Both tunnels feature an inner cross-sectional area of 60.47 m^2 and a hydraulic diameter of 7.77 m. The longitudinal gradient follows a V-shape profile; for the Boryeong-bound tunnel, this includes a 1810 m descent at −4.95%, a 3080 m section at +0.5%, and a 2027 m ascent at +4.85%.

The ventilation system is a longitudinal jet fan type, with 41 jet fans (Φ 1030 mm × 30 kW, outlet velocity of 34 m/s) installed in each direction. An overview of the major facility installation is shown in Figure 1, and the tunnel specifications are summarized in Table 1.

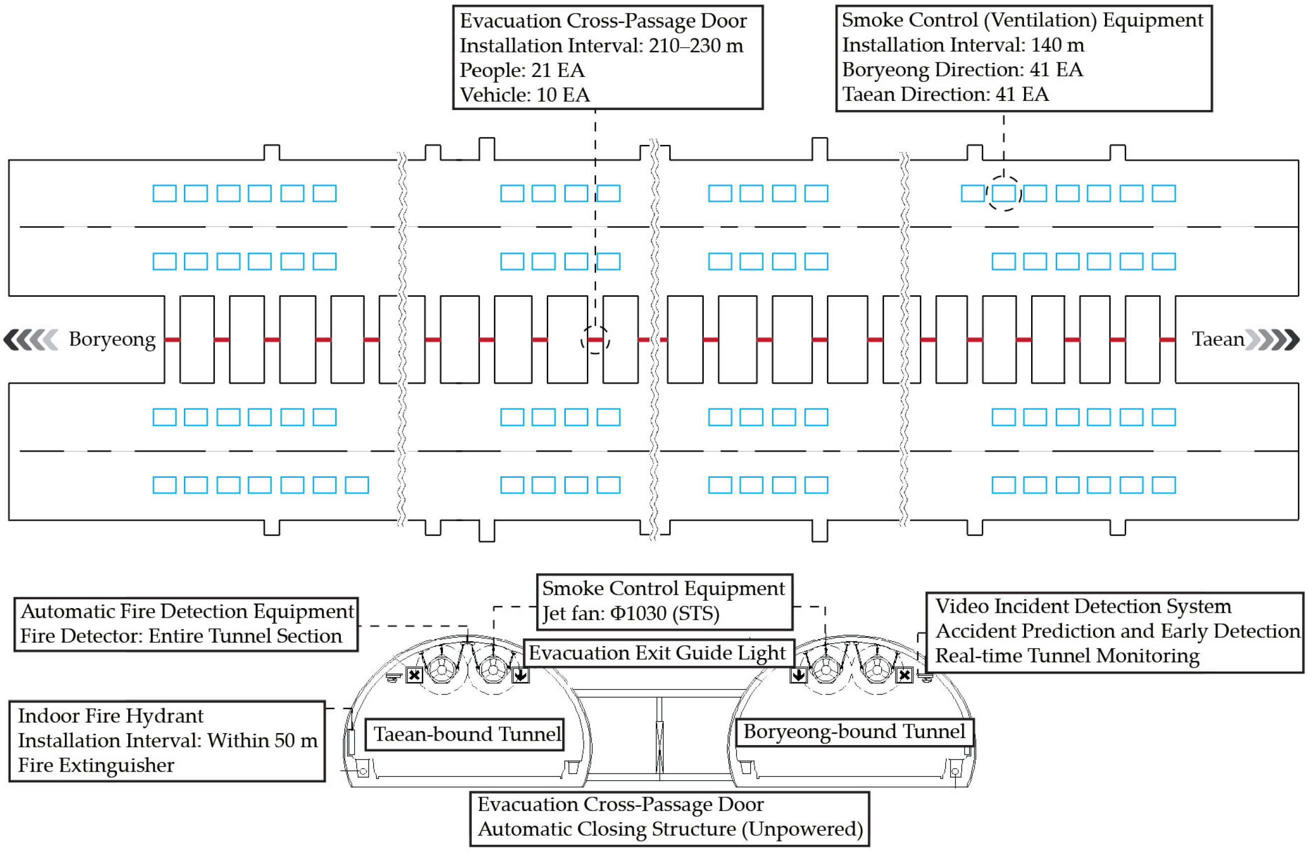

Figure 1. Overview of major facility installation and longitudinal profile of Boryeong Subsea Tunnel.

Table 1. Summary of Boryeong Subsea Tunnel specifications.

Item	Boryeong Direction	Taean Direction
Length (m)	6916	6927
Inner cross-sectional area (m^2)	60.47	60.47
Hydraulic diameter (m)	7.77	7.77
Longitudinal gradient (%)	−4.95/+0.5/+4.85	−4.85/−0.5/+4.95
Traffic type	One-way, 2 lanes	One-way, 2 lanes
Design traffic volume (in 2037)	12,903 veh/day	12,903 veh/day
Jet fan installation	Φ 1030 × 41 units	Φ 1030 × 41 units

2.2. Climate Conditions and Condensation Observations

The Boryeong Subsea Tunnel is located in a coastal area influenced by a maritime climate, characterized by typically hot, humid summer conditions. Analysis of meteorological observations at the nearby Daecheonhang Automated Weather Station (AWS) shows that the monthly average outdoor air temperature (T_d) and relative humidity (RH) during July–August exceed 25 °C (with peaks above 34 °C) and 85%, respectively. Relative humidity is typically even higher than 90% during nighttime. Table 2 summarizes the monthly average meteorological modeling input data and dew point temperature analysis results. Condensation is predicted to occur from May to September when the dew point temperature (T_{dp}) exceeds the ground temperature (T_g). A maximum difference ($T_{dp} - T_g$) of 11.34 °C was observed in July.

Table 2. Monthly average weather modeling input data and condensation occurrence condition analysis results.

Month	**Ambient Air**		**Ground Temperature**	**T_{dp} (°C)**	**$T_{dp} - T_g$ (°C)**
	T_d (°C)	**RH (%)**	**T_g (°C)**		
January	−0.8	61.3	16.7	−8.47	−25.17
February	2.16	64.26	15.58	−4.91	−20.49
March	7.41	69.51	14.54	1.44	−13.10
April	13.92	76.02	13.87	9.40	−4.47
May	20.39	82.49	13.74	17.24	3.50
June	25.52	87.62	14.20	23.36	9.16
July	28.27	90.37	15.12	26.46	11.34
August	28.11	90.21	16.25	25.88	9.63
September	25.05	87.15	17.28	21.76	4.48
October	19.72	81.82	17.93	14.96	−2.97
November	13.18	75.28	18.03	6.90	−11.13
December	6.74	68.84	17.55	−0.65	−18.20

Condensation was first observed approximately five months after opening, in May 2022. Initially, only the lower portion of the sidewalls and the nearby road were wet, but by July, condensation had developed on the sidewalls, floors, and utility ducts throughout the tunnel, as shown in Figure 2.

(**a**) (**b**) (**c**)

Figure 2. Condensation in three different situations: (**a**) after opening~before May—partial wetting on lower side wall; (**b**) in May (condensation occurs)—wetting on side walls, floor, and utility ducts; (**c**) in July (after jet fan operation)—condensation alleviated after jet fan operation.

The CCTV footage at this time clearly shows when condensation occurs. Condensation occurred predominantly during the nighttime and early morning hours (21:00–06:00), when the outdoor humidity reached maximum levels and traffic volume was minimal, with alleviation observed during the daytime hours, when solar heating reduced the outdoor relative humidity. In the most severe cases, fog formed inside the tunnel, significantly reducing visibility, and tunnel users raised safety concerns, misidentifying the condensation as structural water leakage. Condensation occurrence by time period based on CCTV monitoring is presented in Figure 3.

Figure 3. Photos of condensation by time period in the Boryeong Subsea Tunnel: (**a**) Taean 6.0 km 18:30—onset; (**b**) Taean 6.0 km 01:00—peak; (**c**) Taean 6.0 km 07:50—end.

3. Methodology

3.1. Field Measurements

Field measurements were conducted over 14–15 August 2023 in the Boryeong-bound tunnel. Field data measurements were conducted during the summer season, when condensation phenomena are most severe, and it was confirmed that condensation occurred over almost the entire length of the tunnel at the time of measurement. Measurement items included external meteorological conditions (atmospheric pressure, temperature and humidity, and wind direction and velocity) and variables affecting the thermal environment inside the tunnel (traffic volume, atmospheric pressure, tunnel airflow direction, air velocity, air temperature, humidity, wall temperature, vehicle speed, and vehicle type). As shown in Figure 4, measurements were carried out at a total of three locations: one external station situated outside the Taean-side tunnel portal and two internal stations at evacuation passages #5 and #3 within the Boryeong-bound tunnel, located at distances of 4 km and 5.3 km from the portal, corresponding to approximately 58% and 77% of the total tunnel length, respectively. These measurement points were specifically selected near the cross-passages of the twin-tube tunnel in order to ensure the personal safety of the field researchers conducting measurements inside the operational tunnel with active vehicle traffic. The air temperature inside the tunnel was measured using a piezoelectric sensor (Bosch, BME680, Reutlingen, Germany) integrated into a data logger, as well as a separate thermocouple-type wall thermometer (Gain Express AZ Instruments, Model A0188598, Hong Kong, China). In addition, three multi-channel hot-wire anemometers (E+E Elektronik, Model EE650, Engerwitzdorf, Austria) were installed, with data sampled at 1 s intervals and processed as averaged values. The data logger processed the continuously input signals at a resolution of 10 bits, averaging the signals over each 1 s interval.

The measurement data show that the ambient air temperature in the Taean-bound tunnel ranged from 26.4 to 34.7 °C, relative humidity from 68.7 to 94.0%, and atmospheric pressure from 100.5 to 100.7 kPa, while inside the tunnel, the air temperature ranged from 22.5 to 24.2 °C, relative humidity from 87.8 to 94.1%, and air velocity from 0.2 to 4.5 m/s. Traffic volume was in the range of 3 to 522 vehicles/h. Ventilation jet fans were operated from 13:40 to 17:10 on August 14, and tunnel air velocity increased from approximately 2.5 m/s to 4.5 m/s after fan operation.

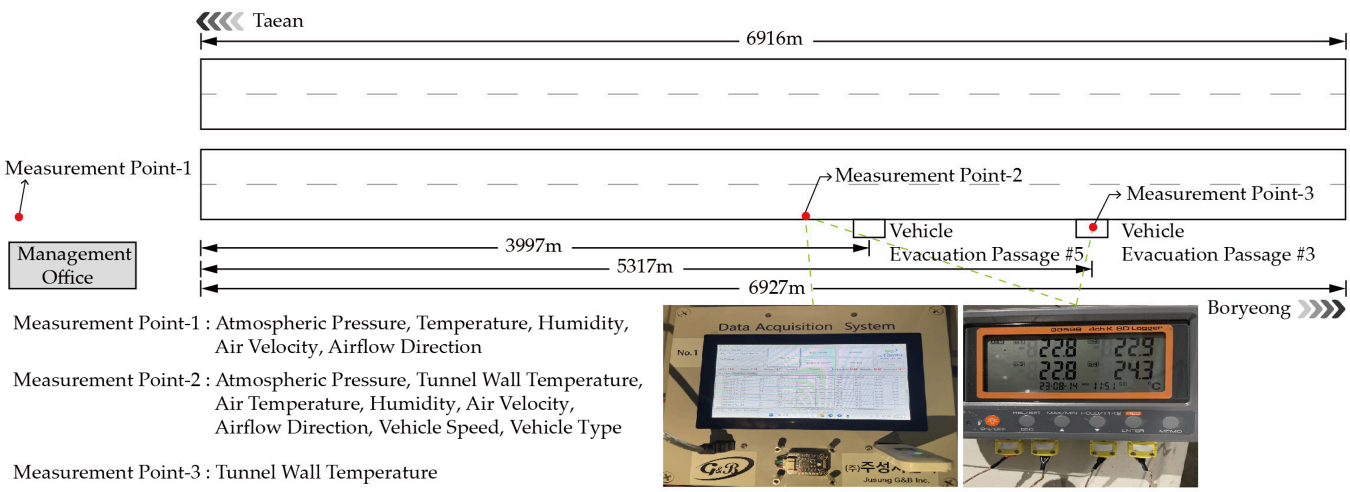

Figure 4. Field measurement overview.

3.2. One-Dimensional Thermodynamic Model

Figure 5 presents a conceptual diagram of the heat and moisture transfer occurring among the tunnel airflow, the tunnel inner wall surface, and the moving vehicles inside the tunnel.

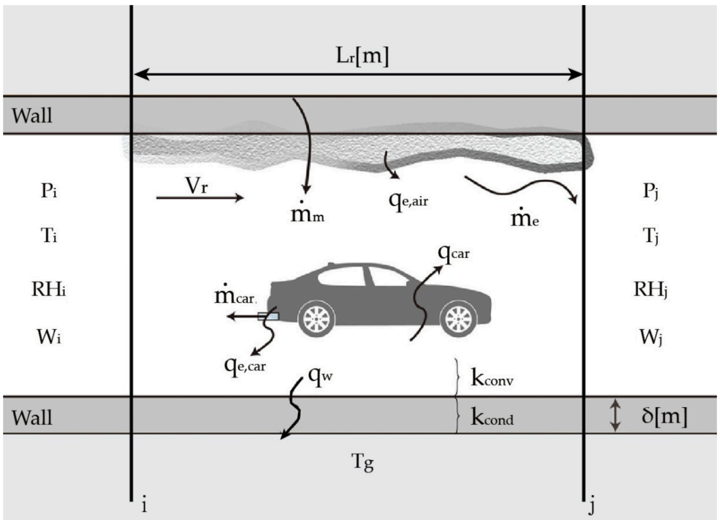

Figure 5. Conceptual diagram of heat transfer and moisture transmission within the analysis section.

In the model, one-dimensional nodal points are established at regular intervals, and at each node, the following parameters are computed: air temperature and humidity (relative humidity and absolute humidity) inside the tunnel, dew point temperature, wall surface temperature, condensate amount, and evaporation rate in wetted surface areas. The computational procedure adopted for the estimation of condensate quantity is described in the following steps:

Step 1: The air temperature at each nodal point is determined by applying the energy balance equation (Equation (1)), which states that the sum of vehicle heat generation and the latent heat of moisture, minus the heat loss through the tunnel wall, is equal to the sensible heat change of the airflow. The energy balance equation incorporates four heat transfer mechanisms: (i) air-to-wall convective heat transfer; (ii) heat gain from vehicles, modeled as a distributed source proportional to traffic intensity; (iii) latent heat exchange from wet surfaces and vehicle moisture; and (iv) conductive heat transfer through the tunnel wall to the surrounding ground.

$$A_w = \mathrm{P} \cdot L_r = \frac{4 \cdot A_r}{D} \cdot L_r$$

$$A_m = A_w \cdot \frac{Moisture\ Rate\ (\%)}{100}$$

$$\dot{m}_{m,total} = \dot{m}_m \cdot A_m + \dot{m}_{car}$$

$$\dot{m}_{e,total} = \dot{m}_e \cdot A_m$$

$$Q_w = q_w \cdot A_w$$

$$Q_{car} = q_{car} \cdot L_r$$

$$Q_e = q_{e,air} + q_{e,car}$$

$$Q_{car} + Q_e - Q_w = \dot{m} C_p \left(T_j - T_i\right) \quad (1)$$

where

L_r: Reference tunnel length (m);

P: Perimeter of the tunnel inner wall surface (m);

$P_{i,j}$, $T_{i,j}$, $RH_{i,j}$, $W_{i,j}$: Pressure, temperature, relative humidity, and absolute humidity at nodes i and j (Pa, °C, %, kg/kg);

A_W: Area of the tunnel inner wall surface (m^2);

A_m: Moist area (m^2);

$\dot{m}_{car,total}$: Moisture transmission rate from a vehicle exhaust outlet (kg/s);

$\dot{m}_{m,total}$: Moisture transmission rate from a moist area (kg/s);

$\dot{m}_{e,total}$: Convective evaporation rate (kg/s);

k_{conv}: Thermal conductivity of the air (W/m·K);

k (or k_{cond}): Equivalent thermal conductivity of the composite wall (W/m·K);

δ : Equivalent thickness of the composite wall (m);

Q_w: Total tunnel wall heat flux (W);

Q_{car}: Total vehicle heat release rate (W);

Q_e: Total latent heat of evaporation (W);

$q_{e,air}$: Latent heat of evaporation from vehicle exhaust (W);

$q_{e,car}$: Latent heat of evaporation from moist wall (W);

C_p: Specific heat capacity of air at constant pressure (J/kg·K).

Step 2: In the absence of evaporation and condensation, the absolute humidity of the tunnel air remains constant, and the relative humidity and dew point temperature are computed based on the prevailing temperature conditions. The dew point temperature is determined through an iterative calculation procedure, in which the equilibrium temperature is sought such that the difference between the partial pressure of water vapor and the saturation vapor pressure at the given state point satisfies the prescribed convergence criterion of 10^{-3}. By introducing the concept of thermal resistance (R_{th}), the heat flux can be expressed as the ratio of the difference in thermal potential to thermal resistance. The wall temperature (T_w) is then calculated by considering the overall heat transmission from the ground temperature and the tunnel air temperature, as in Equation (3).

$$R_{th} = 1/h + \delta/k_{cond},\ 1/h = D/(k_{conv} \cdot \mathrm{Nu}) \quad (2)$$

$$T_w = \frac{T_a + \left[\frac{k}{\delta} \cdot R_{th} - 1\right] \cdot T_g}{\left(\frac{k}{\delta}\right) \cdot R_{th}} \quad (3)$$

https://doi.org/10.3390/infrastructures11060209

where

T_w: Temperature of the tunnel wall surface (°C);

T_a: Temperature of the inside tunnel air (°C);

T_g: Ground temperature, assumed to be constant at 15 °C;

R_{th}: Total thermal resistance ($m^2 \cdot K/W$);

h: Forced-convective heat transfer coefficient ($W/m^2 \cdot K$);

D: Hydraulic diameter of the tunnel (m);

Nu: Nusselt number, determined using the Gnielinski correlation [24].

The thermal conductivity characteristics of the tunnel wall surface are critical parameters in the mechanism of air-to-wall convective transfer. Generally, the tunnel wall consists of three composite layers: a lining (concrete), a waterproof membrane (mainly an HDPE sheet), and shotcrete. Table 3 shows the thermal properties of the individual and composite layers; the equivalent thermal conductivity of the composite layer (k) is 1.705 W/m·K, with an equivalent thickness (δ) of 0.602 m and an overall thermal transmittance (U-value) of 2.832 $W/m^2 \cdot K$. Vehicle heat generation is modeled as a distributed source using calorific values of 30.4 MJ/L for gasoline and 35.2 MJ/L for diesel (Korean Energy Act). Exhaust water vapor output from vehicles is assumed to be 1.1 L water per 1 L fuel (Kibble, 1978) [25].

Table 3. Thermophysical properties and thermal transmittance of the tunnel wall structure.

Wall Composition	Thermal Conductivity (W/m·K)	Thickness (m)	Thermal Resistance ($m^2 \cdot K/W$)	Remarks
Lining (concrete)	2.50	0.45	0.180	Inside waterproof layer
Waterproof membrane	0.024	0.002	0.083	HDPE type
Shotcrete	1.67	0.15	0.090	NATM support
Composite total	1.705	0.602	0.353	—
Overall thermal transmittance (U-value)	—	—	—	2.832 $W/m^2 \cdot K$

Step 3: Condensation is assumed to occur when the dew point temperature (T_{dp}) exceeds the temperature of the tunnel wall surface (T_w). The condensation rate ($\dot{m}_{cond}$) can be estimated based on the measurement data of the atmospheric pressure, ambient air dry and wet temperatures, inside air temperature, tunnel wall temperature, and tunnel air velocity as follows:

$$w = 0.622 \times (RH/100) \times e_s \, / \, (P_{atm} - (RH/100) \times e_s) \quad (4)$$

$$w_{sat}(T_w) = a_0 + a_1 T_w + a_2 {T_w}^2 + a_3 {T_w}^3 \quad (5)$$

$$\dot{m}_{cond} = \rho \cdot V \cdot A \cdot (w - w_{sat}(T_w)) \quad (6)$$

where

w: Absolute humidity (kg/kg (DA));

$w_{sat}(T_w)$: Saturated absolute humidity (w_{sat}) at the wall temperature (T_w) (kg/kg (DA));

$\dot{m}_{cond}$: Condensation mass rate (kg_{water}/s);

P_{atm}: Atmospheric pressure (Pa);
e_s: Saturated vapor pressure (Pa);
a_{0-3}: Curve-fitting coefficient;
V: Tunnel longitudinal air velocity (m/s);
A: Tunnel inner cross-sectional area (m^2).

3.3. Three-Dimensional CFD Simulation

Three-dimensional CFD simulations were performed using OpenFOAM v10, an open-source computational fluid dynamics (CFD) software package used for simulating fluid flow, heat transfer, and related physical processes. The computational domain represented the entire tunnel length of 6.9 km using the actual cross-sectional geometry. Because the tunnel cross-section is approximately symmetric, only a half-section was analyzed, and the results were mirrored about the symmetry plane for presentation. The CFD model and computational grid are shown in Figure 6.

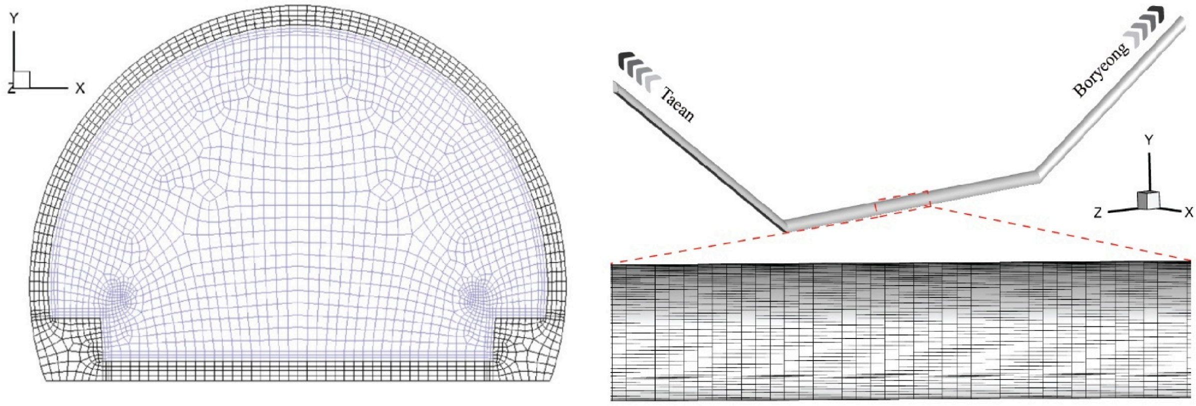

(**a**) (**b**)

Figure 6. Three-dimensional CFD analysis model and grid: (**a**) cross-sectional view; (**b**) full-length view.

The Reynolds-averaged Navier–Stokes (RANS) equations for continuity, momentum, energy, and humidity transport were solved in steady-state mode. Turbulence was modeled using the standard k–ε model [26], which provides robust and computationally efficient predictions of the mean flow and heat transfer characteristics in large-scale internal flows. Pressure–velocity coupling was handled by the SIMPLE (Semi-Implicit Method for Pressure-Linked Equations) algorithm [27]. Convective terms were discretized using a second-order upwind scheme, while diffusive terms were treated with central differencing to ensure numerical accuracy.

The discretized computational grid consisted of approximately 74 million polyhedral cells (74,073,710), generated as elongated cylindrical elements along the tunnel axis. The standard k–ε turbulence model was adopted in this CFD analysis. The resulting y+ values ranged from 152.80 to 213.99, satisfying the recommended range of 30 < y+ < 300 for the standard k–ε model [28].

The convergence time is defined as the computational time required for the residuals to fall below the prescribed tolerance and for the variations in the primary physical quantities to become sufficiently small throughout the iterative solution process. All simulations were conducted on a computer with Intel® Xeon® 2.1 GHz, 2CPU, 16 Core specifications. The initial baseline case for the simulation analysis reached convergence in approximately 14 days. And subsequent computations, which utilized the converged baseline as an initial solution, required between 72 and 120 h to reach steady-state convergence. Convergence was monitored using the residuals of all governing equations, with thresholds of 10^{-4} for continuity and momentum and 10^{-6} for energy and humidity transport.

The boundary conditions for the CFD model were prescribed as follows: a uniform velocity, temperature, and humidity profile at the inlet and a pressure outlet condition at the tunnel exit. For the external wall, a depth-dependent temperature profile was implemented, originating from an ambient temperature of 25 °C. The temperature was assumed to decrease at a rate of 0.08 °C/m in the landward sections, while this gradient was doubled to 0.16 °C/m within the subsea portion, resulting in a minimum outer-wall temperature of 11.54 °C at the tunnel's lowest elevation. The thermal conductivity of the composite wall and the lining thickness were set to 1.7 W/m·K and 0.5 m, respectively. The baseline simulation scenario for July was analyzed with an inlet temperature of 28.27 °C, relative humidity of 90.37%, and inflow velocity of 2.5 m/s.

In the CFD analysis of this study, neither a separate transport model nor a User-Defined Function (UDF) was employed; instead, the logic of the so-called Equilibrium Condensation Model was applied. Accordingly, it was assumed that condensation occurs when the relative humidity at the grid points near the wall exceeds 100%, and the amount of condensation was determined by the excess absolute humidity over the saturated absolute humidity. Therefore, the present CFD analysis should be interpreted as an approximate study of humidity distribution rather than a fully coupled condensation simulation.

4. Results and Discussion

4.1. Field Measurement Results

The field measurement results showed wall temperatures of 22.1–23.6 °C at location #5 (4.0 km from the Taean-bound tunnel) and 20.7–22.4 °C at location #3 (5.3 km from the Taean-bound tunnel). The tunnel wall temperature decrease rate in the flow direction was approximately 0.97 °C/km, and the air–wall temperature difference remained nearly constant at approximately 1.5 °C throughout the measurement period. The effect of jet fan operation was clearly observed; after fan activation at 13:40, the tunnel air velocity increased from 2.58 to 4.41 m/s. The absolute humidity at the measurement locations increased during fan operation, which is interpreted as the result of an enhanced evaporation phenomenon from upstream wet wall surfaces, leading to increased moisture inside the tunnel. After jet fan shutdown, the absolute humidity decreased rapidly, confirming a quick return to net condensation conditions. This indicates that, while jet fan operation can shift the condensation front downstream, it cannot completely eliminate condensation when the incoming air is already near saturation. The measurement results of the air velocity, temperature, and humidity before and after jet fan operation are presented in Figure 7.

4.2. Comparison of the 1D Model Against the Psychrometric Analysis

It is challenging to evaluate whether the 1D model predictions fully satisfy fundamental moist air thermodynamics, and this is particularly true when simultaneously accounting for the heat and moisture transfer induced by vehicle traffic inside the tunnel. Therefore, taking suggestions into consideration, we compare the 1D model predictions with the results of a psychrometric analysis under a relatively simplified scenario. This comparison can be seen in the Section 5 evaluating the 1D model.

The analyzed scenario is based on a tunnel inlet atmospheric pressure of 101.3 kPa, an inlet airflow velocity of 2.65 m/s, a ground temperature (T_g) of 15 °C, and an inlet relative humidity (RH) of 70%. Figure 8a shows the profiles of the tunnel air temperature (T_a) and wall temperature (T_w) from the tunnel inlet to the outlet, as analyzed by the 1D model. At the tunnel outlet, T_a and T_w are 16.20 °C and 16.04 °C, respectively, with an RH of 100%. Figure 8b presents the profiles of the absolute humidity (black dashed line with 'x' symbols) and the condensation rate (red curve) inside the tunnel obtained from the 1D model. The total condensation rate, which corresponds to the area under the condensation rate curve, is 1.325 kg/s.

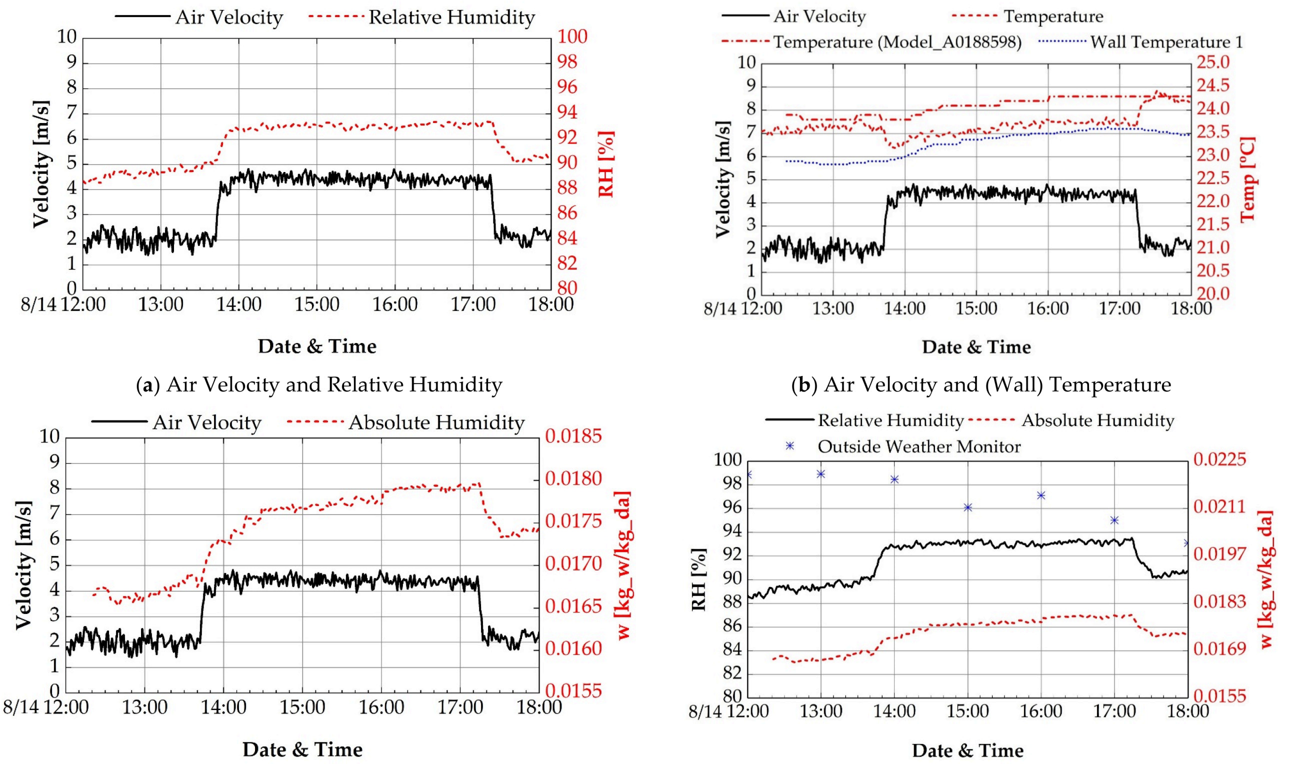

(**a**) Air Velocity and Relative Humidity (**b**) Air Velocity and (Wall) Temperature

(**c**) Air Velocity and Absolute Humidity (**d**) Relative Humidity and Absolute Humidity Inside the Tunnel

Figure 7. Measurement profiles of air velocity, temperature, and humidity before and after jet fan operation.

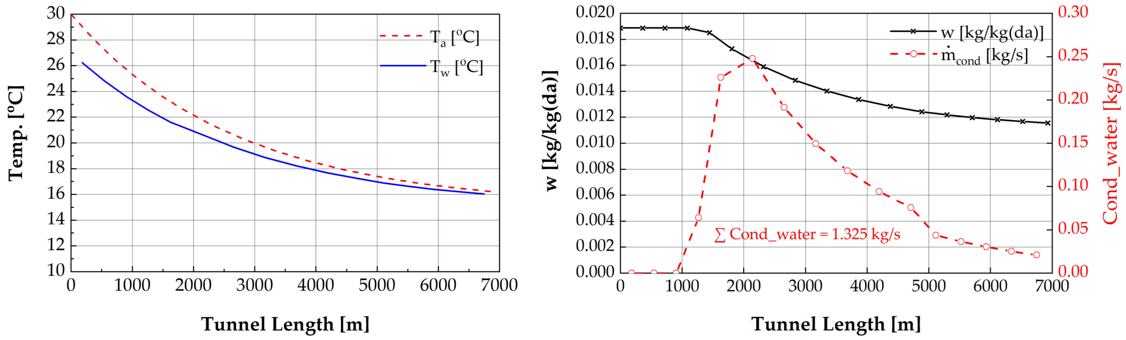

(**a**) (**b**)

Figure 8. One-dimensional model analysis results: (**a**) temperature profiles; (**b**) absolute humidity and condensation volume profiles.

Meanwhile, to estimate the total condensation rate in the tunnel using a psychrometric chart, the state points defined by the temperature (T_a) and RH at the inlet and outlet obtained from the 1D model results are plotted in Figure 9. The absolute humidities at State Points 1 and 2 are 0.0188 kg/kg and 0.0115 kg/kg, respectively. Assuming that the total condensation rate equals the mass flow rate of air in the tunnel (181.13 kg/s) multiplied by the difference in absolute humidity between the inlet and outlet (0.0188–0.0115 kg/kg), it is estimated to be 1.317 kg/s. Consequently, the daily condensation amounts derived from the 1D model and the psychrometric analysis are 114.45 ton/day and 113.77 ton/day, respectively, demonstrating a relatively small difference of 0.68 ton/day.

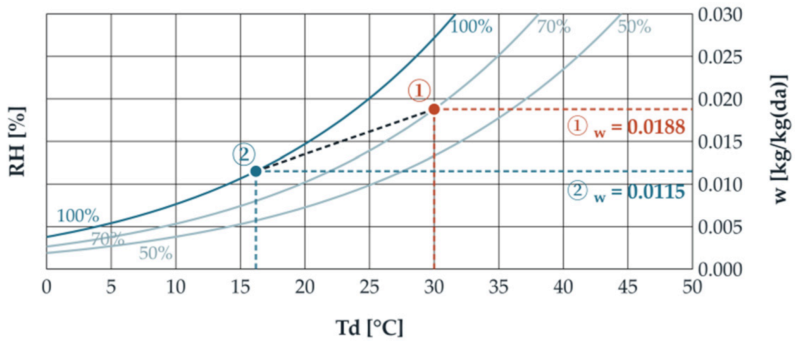

Figure 9. Psychrometric chart analysis results.

4.3. Comparison of the 1D Model Against Field Data

The accuracy of the 1D model was verified against field measurements at 13:00 (before jet fan operation) and 15:00 (after operation) on 14 August 2023. The boundary conditions for the case of 13:00 were an ambient temperature of 34.14 °C, relative humidity of 72.81%, and tunnel air velocity of 2.58 m/s; at 15:00, these values were 34.70 °C, 68.71%, and 4.41 m/s, respectively. As shown in Table 4, the inside air temperature errors ranged from 3.0 to 7.3% (≤1.67 °C), and the wall temperature errors ranged from 0.8 to 7.3% (≤1.58 °C), demonstrating good agreement between the model and the measurements. A comparison between the measured and predicted results is shown in Figure 10.

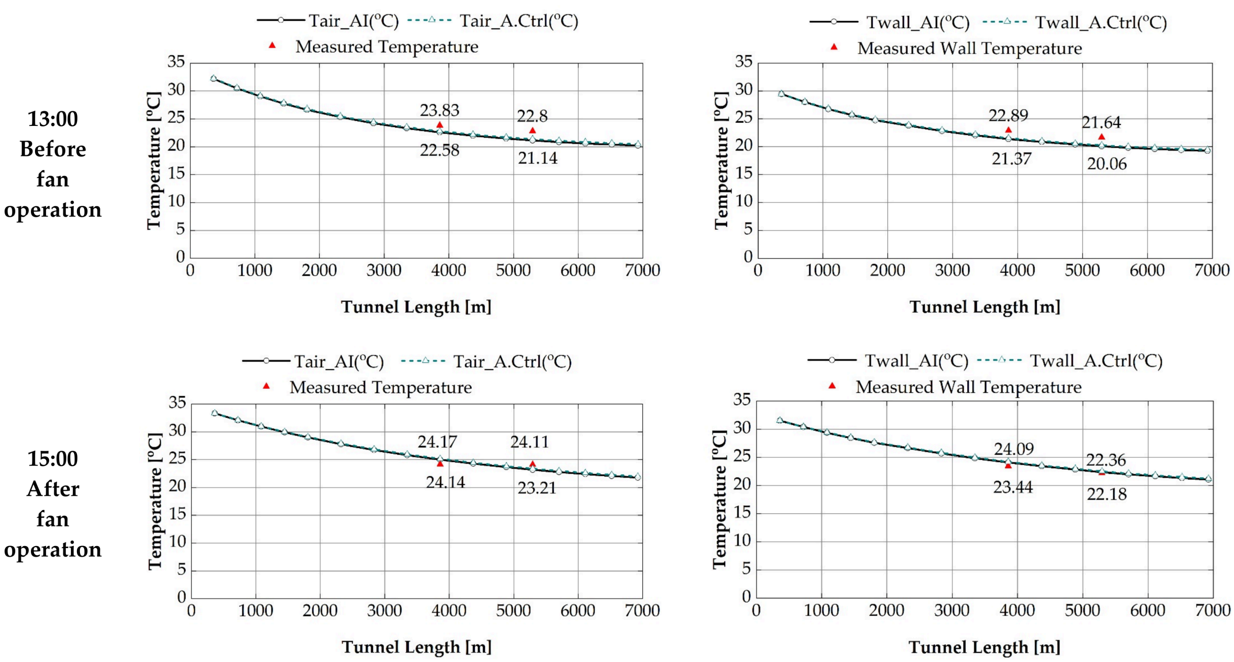

(**a**) Inside Air Temperature (**b**) Wall Temperature

Figure 10. Comparison of measured profiles and 1D analytical results.

A quantitative comparison was derived from the eight measurement–prediction pairs listed in Table 4. The root mean square error (RMSE) was 1.24 °C for the inside air temperature and 1.16 °C for the wall temperature. The mean absolute error (MAE) was 1.10 °C and 1.02 °C, respectively. The coefficient of determination (R^2) exceeded 0.92 for both parameters, confirming that the 1D model reproduces longitudinal temperature gradients with acceptable accuracy for engineering applications.

Table 4. Comparison of measured values and 1D analytical values.

Time	Location	Item	Measured (°C)	Analytical (°C)	Error (%)
13:00	4.0 km	Inside Air Temp.	23.83	22.58	5.2
13:00	5.3 km	Inside Air Temp.	22.80	21.14	7.3
13:00	4.0 km	Wall Temp.	22.89	21.37	6.6
13:00	5.3 km	Wall Temp.	21.64	20.06	7.3
15:00	4.0 km	Inside Air Temp.	24.17	25.01	3.5
15:00	5.3 km	Inside Air Temp.	24.11	23.21	3.7
15:00	4.0 km	Wall Temp.	23.44	24.09	2.8
15:00	5.3 km	Wall Temp.	22.18	22.36	0.8

4.4. Comparison of 1D Model and CFD Results

To further assess the reliability of the 1D model, the results were compared with the CFD results under the same boundary conditions, specifically a uniform outer wall temperature of 15.12 °C and wall thermal conductivity of 1.7 W/m·K. The distributions of the inside air temperature, wall temperature, and condensation volume along the tunnel axis showed very good agreement between the two approaches. In the case of the 3D CFD results, under the baseline conditions (28.27 °C, 90.37% RH, and 2.5 m/s), the relative humidity reached 100% at approximately 2.0 km from the Taean-bound tunnel, and supersaturated conditions developed farther downstream. A comparison of the condensation volume between the 1D analysis and the 3D CFD analysis under zero-traffic conditions is shown in Figure 11.

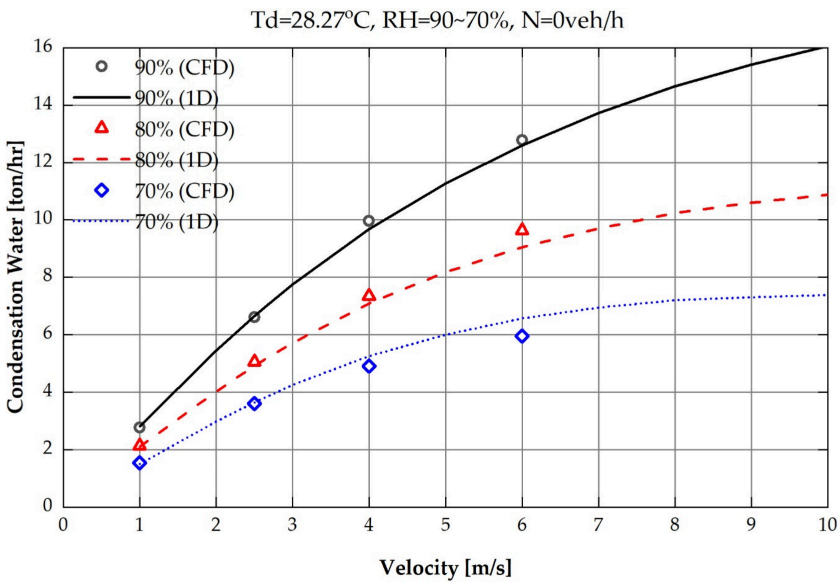

Figure 11. Comparison of condensation water volume between 1D analysis and 3D CFD analysis by relative humidity.

4.5. Condensation Volume Analysis

The monthly condensation-onset locations (distance from the inlet portal of the Taean-bound tunnel) and daily condensation volumes under varying traffic conditions are summarized in Table 5. At an inside air velocity of 2.65 m/s, increasing traffic volume shifts the condensation-onset point farther downstream and reduces the condensation volume. Under the design traffic capacity of 1550 veh/h, no condensation is predicted.

Table 5. Condensation location and volume by traffic conditions (V = 2.65 m/s).

Month	0 veh/h		500 veh/h		1000 veh/h		1550 veh/h	
	km	Tons/Day	km	Tons/Day	km	Tons/Day	km	Tons/Day
May	1.8	36.3	6.9	0.4	—	—	—	—
June	0.7	117.5	1.0	80.1	4.3	18.8	—	—
July	0.7	166.4	0.7	125.8	1.8	60.2	—	—
August	0.5	150.1	1.0	105.0	3.3	33.5	—	—
September	1.0	74.2	3.3	24.6	—	—	—	—

4.6. Annual Condensation Volume Estimation and Traffic Volume Effect

Annual condensation volumes were analyzed as a function of hourly traffic volume at an inside air velocity of 2.65 m/s using full-year meteorological data, as summarized in Table 6. As traffic volume increases from 0 to 250 veh/h, the annual condensation volume decreases by approximately 26%; at 1000 veh/h, it decreases by approximately 96% to only 628 ton/year. At the design traffic capacity of 1550 veh/h, the wall temperature remains above the dew point because of vehicle heat generation, and condensation is completely suppressed.

Table 6. Annual condensation volume by hourly traffic volume (V = 2.65 m/s).

Traffic Volume (veh/h)	Annual Volume (Tons/yr)	Max Daily (Tons/Day)	Reduction vs. Baseline (%)	Condensation Period
0	16,846	172.1	(Baseline)	May–Sep
250	12,415	143.2	26.3	May–Sep
500	7978	108.9	52.6	May–Sep
1000	628	20.9	96.3	Jun–Aug
1550 (Design)	0	0	100.0	None

Using the monthly average meteorological data and the current traffic volume—peaking at approximately 250 veh/h, roughly 16% of the design traffic capacity—as inputs to the 1D model, the annual condensation volume was estimated to be approximately 12,415 ton/year, with the highest level of 143 ton/day. Condensation occurs from May to September, and approximately 85% of the annual total is concentrated in July and August. The monthly condensation volume trends for different traffic levels are shown in Figure 12.

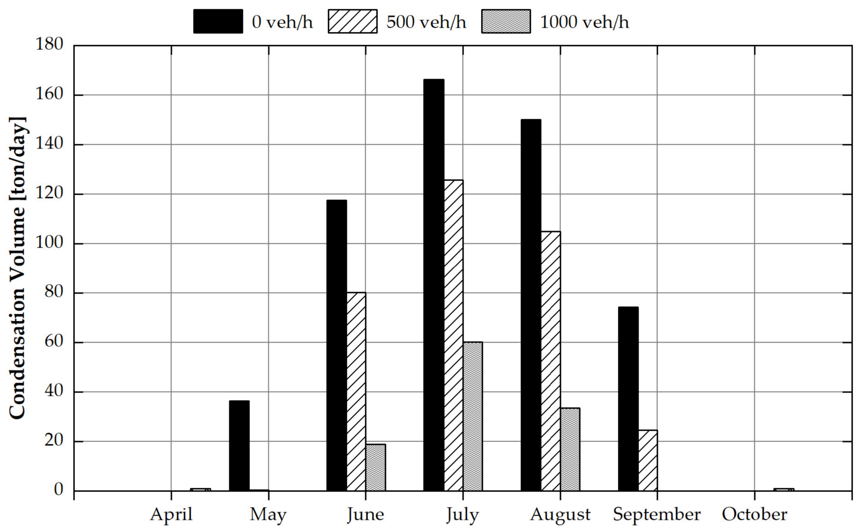

Figure 12. Monthly condensation volume by traffic volume.

4.7. Condensation Contour Map (CCM)

The Condensation Contour Map (CCM) in Figure 13 was developed as a practical decision support tool for design and operation. The CCM illustrates the predicted contour lines for the condensation volume (ton/day) in black and the maximum relative humidity at the tunnel outlet portal (%) in red; in the diagram, the inlet dry-bulb temperature (T_d) is presented on the horizontal axis and the inlet relative humidity is presented on the vertical axis for various air velocities and traffic volumes.

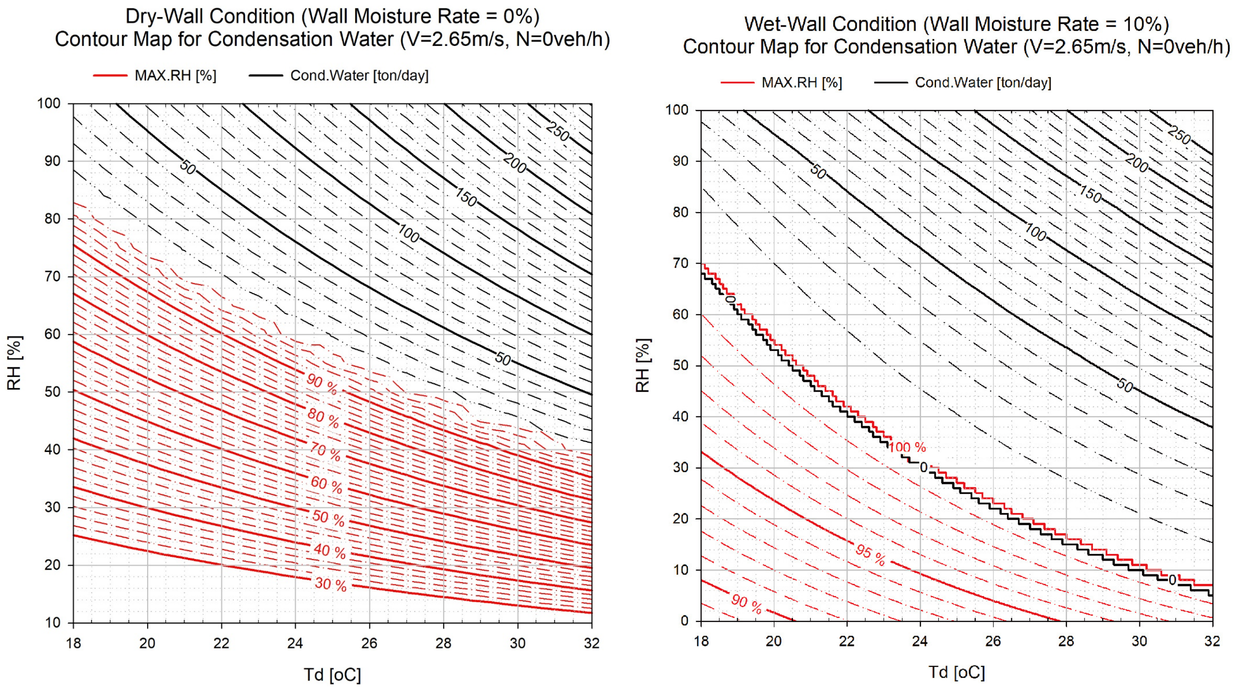

(**a**) Condensation Volume under Dry-Wall and Wet-Wall Conditions with Zero Traffic Volume

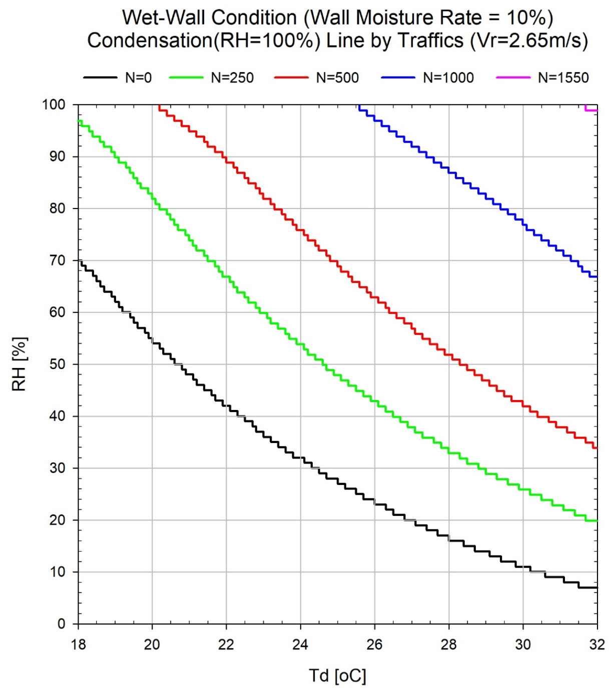

(**b**) Condensation boundary lines (RH = 100%) for different traffic volumes in the Td-RH plane (V = 2.65 m/s)

Figure 13. Condensation Contour Map (CCM): (**a**) contour maps of condensation volume and maximum outlet relative humidity for N = 0 under dry wall and wet wall conditions; (**b**) condensation boundary (RH = 100% line) for varying traffic volumes at V = 2.65 m/s.

https://doi.org/10.3390/infrastructures11060209

The CCM shows that, under current traffic conditions (peaking at 250 veh/h) and an air velocity of 2.65 m/s, condensation occurs when the ambient temperature and relative humidity exceed 24 °C and 80%, respectively. As the traffic volume increases, the condensation boundary shifts toward higher temperature and humidity conditions, confirming the beneficial effect of vehicle heat generation. At the design traffic capacity of 1550 veh/h, condensation occurs only under extreme conditions of $T_d > 30$ °C and RH > 95%, implying that the condensation problem will naturally diminish as the traffic volume increases.

The contour map in Figure 13a for N = 0 shows that substantial condensation volumes are predicted across a wide range of ambient conditions when there is no traffic. Under zero-traffic conditions (N = 0), the condensation boundary starts at an inlet dry-bulb temperature as low as approximately 18 °C at RH ≈ 70%, indicating that condensation can occur even under moderate ambient humidity conditions. Without the heat inflow from vehicles, the temperature is governed exclusively by the surrounding seawater and ground, leading to the widest condensation-prone region. This scenario corresponds to periods of nighttime, early morning, or maintenance closures, during which the tunnel is most vulnerable to condensation.

Figure 13b shows the condensation boundary contours (RH = 100%) as a function of the inlet dry-bulb temperature and relative humidity for five traffic volumes (N = 0, 250, 500, 1000, and 1550 veh/h) at V = 2.65 m/s, with a wall moisture rate of 10%. The area above each curve represents the condensation zone, where the wall temperature falls below the dew point temperature of the tunnel air.

As the traffic volume increases to N = 500 veh/h, vehicle exhaust heat raises the tunnel air and wall temperatures, and the condensation boundary shifts markedly to the right; condensation begins only when the inlet dry-bulb temperature exceeds approximately 20 °C at RH = 100%. At N = 1000 veh/h, the boundary moves further to the right, with condensation initiating only above an inlet dry-bulb temperature of approximately 25.5 °C at RH = 100%, meaning that only high-temperature, high-humidity summer conditions can trigger condensation. At the design traffic capacity of N = 1550 veh/h, the boundary is pushed almost entirely off the chart, the typical operational range. Only a marginal region persists at the extreme upper-right corner of the diagram ($T_d > 31.5$ °C, RH ≈ 100%), confirming that condensation is virtually eliminated under standard climatic conditions. The progressive rightward shift of the boundary from N = 0 to N = 1550 quantitatively demonstrates that vehicle heat generation serves as a natural and highly effective suppression mechanism against condensation.

The results show that even with 145 dehumidifiers currently installed in the tunnel—offering a total capacity of 24.4 tons/day at an 80% utilization rate—only 7.2% of the estimated peak condensation load (roughly 340 tons/day for both directions combined under the 250 veh/h scenario) can be treated. This result underscores that mechanical dehumidification, in its current configuration and scale, is insufficient to provide a standalone solution for moisture mitigation.

5. Conclusions

The purpose of this study was not to theoretically analyze condensation phenomena in operating tunnels but rather to develop engineering solutions for the condensation issues that cause severe safety concerns in the Boryeong Undersea Tunnel, South Korea's longest undersea tunnel (6.9 km). On-site measurements, one-dimensional thermodynamic model development and analysis, and three-dimensional CFD simulations were employed in this study, and the results are summarized as follows:

(1) Condensation in the Boryeong Subsea Tunnel results from the combined effect of a hot, humid maritime climate at the portals and low wall temperatures caused by the surrounding seawater and ground. The condensation phenomenon that occurs in the tunnel differs fundamentally from structural water leakage commonly addressed in tunnel engineering and therefore necessitates a specialized analytical approach and tailored operational strategies.

(2) The developed 1D model showed high predictive accuracy, with air and wall temperature discrepancies within 7.3% of the field measurements. It also showed excellent agreement with the 3D CFD results, validating its efficacy as an efficient engineering tool for rapid parametric analysis. The mutual consistency among the field data and the results of the thermodynamic analysis based on 1D and 3D models provides a rigorous basis for comprehensive cross-validation.

(3) Under high-humidity conditions, increasing the air velocity in the tunnel by jet fan operation was found to aggravate condensation. Accordingly, operating at lower ventilation rates during high-humidity periods, especially on summer nights, may help reduce condensation, whereas jet fan operation during lower-humidity daytime periods may promote evaporation of existing condensate.

(4) Vehicle-induced heat generation is the most effective natural mechanism for condensation suppression. Although condensation is almost entirely eliminated at the design traffic volume of 1550 veh/h, the current traffic volume peaks at approximately 250 veh/h, which is insufficient, indicating the need for supplementary countermeasures during the present operational stage.

(5) The proposed Condensation Contour Map (CCM) provides a practical engineering basis for designers and tunnel operators to predict condensation as a function of ambient air conditions and traffic volume and to make rational decisions regarding jet fan operation and dehumidification strategies. Although the CCM proposed in this study assumes a tunnel air velocity of 2.65 m/s, if the air velocity within the tunnel changes due to tunnel operational factors such as fan control strategies, alarm systems, and dehumidification management, the contour map can be redrawn and utilized accordingly to reflect such changes.

(6) Current ventilation and environmental control systems for subsea tunnels still focus primarily on pollutant control and fire safety, with limited explicit consideration of condensation. The results of this study suggest that future long subsea tunnel design should explicitly consider condensation from the design stage onward, together with mitigation measures such as enhanced wall insulation, rational dehumidification capacity planning, dew point-aware ventilation strategies, and driver warning systems. They also suggest that tunnel ventilation standards and guidelines should clearly address condensation in long subsea tunnels, particularly those located in humid climate regions.

Author Contributions: H.K., Conceptualization, Methodology, Software, Formal analysis, Investigation, Resources, Data curation, Writing—original draft, Writing—review & editing, Visualization, Project administration, Funding acquisition; C.-W.L., Conceptualization, Validation, Formal analysis, Investigation, Writing—review & editing, Supervision. All authors have read and agreed to the published version of the manuscript.

Funding: This research received no external funding.

Data Availability Statement: The data presented in this study are available on request from the corresponding author. The data are not publicly available due to restrictions imposed by the tunnel operating authority.

Conflicts of Interest: Author Hyogyu Kim was employed by the company Jusung G&B Inc. The remaining authors declare that the research was conducted in the absence of any commercial or financial relationships that could be construed as a potential conflict of interest.

References

1. Ministry of Land, Infrastructure and Transport. *Guidelines for Installation and Management of Road Tunnel Fire Safety and Ventilation Facilities*; MOLIT: Sejong, Republic of Korea, 2025.
2. PIARC. *Road Tunnels: Vehicle Emissions and Air Demand for Ventilation*; World Road Association: Paris, France, 2019.
3. Bradbury, W.M.S.; Gill, M.E.; LeCorronc, S. Humidity and Condensation in the Channel Tunnel. In Proceedings of the Channel Tunnel Experience: Lessons for the Future, London, UK, 20–21 March 1997; pp. 37–47.
4. Ikuma, M. Maintenance of the Undersea Section of the Seikan Tunnel. *Tunn. Undergr. Space Technol.* **2005**, *20*, 143–149. [CrossRef]
5. Kawasaki Heavy Industries. *The Opening of Hokkaido Shinkansen: Series H5 Design Challenges—Condensation, Snow, and Icing*; Kawasaki Technical Report; Kawasaki Heavy Industries: Kobe, Japan, 2016.
6. Dangerous Roads. North Cape Tunnel—A Subsea Road Tunnel. Available online: https://www.dangerousroads.org (accessed on 1 January 2024).
7. Norwegian Public Roads Administration. *Rogfast—World's Longest and Deepest Subsea Road Tunnel*; NPRA: Rogaland, Norway, 2024.
8. Lervåg, L.E. *Kartlegging av Faktorer som kan ha Betydning for Kondensdannelse i Tunneler*; SINTEF Report; SINTEF: Trondheim, Norway, 2005.
9. Yan, Q.; Zhang, C.; Lin, G.; Wang, B. Temperature and Moisture Distributions of Long Tunnels and Analysis of Condensation on Tunnel Walls in Hot and Humid Areas. *J. Railw. Eng. Soc.* **2017**, *34*, 65–71.
10. Bopp, R.; Peter, A. Windshield Fogging in Road Tunnels—Final Results. In Proceedings of the 3rd International Conference on Tunnel Safety and Ventilation, Graz, Austria, 15–17 May 2006; pp. 213–220.
11. Yang, B.; Yao, H.; Wang, F. A Review of Ventilation and Environmental Control of Underground Spaces. *Energies* **2022**, *15*, 409. [CrossRef]
12. Park, S.-J.; Lee, I.-B.; Lee, S.-Y.; Kim, J.-G.; Cho, J.-H.; Decano-Valentin, C.; Choi, Y.-B.; Lee, M.-H.; Jeong, H.-H.; Yeo, U.-H.; et al. Air Conditioning System Design to Reduce Condensation in an Underground Utility Tunnel Using CFD. *IEEE Access* **2022**, *10*, 78200–78212. [CrossRef]
13. Tai, C.; Tian, G.; Lei, W.; Wang, J. A Field Measurement of Temperature and Humidity in a Utility Tunnel and a Brief Analysis of the Exhaust Heat Recovery System. *Indoor Built Environ.* **2020**, *30*, 1403–1415. [CrossRef]
14. You, S.; Li, W.; Ye, T.; Hu, F.; Zheng, W. Study on Moisture Condensation on the Interior Surface of Buildings in High Humidity Climate. *Build. Environ.* **2017**, *125*, 39–48. [CrossRef]
15. Ryu, J.; Kim, J.; Ra, K. Numerical Study on Thermal Characteristics According to Wind Speed Changes in Underground Utility Tunnels. *J. Korean Tunn. Undergr. Space Assoc.* **2017**, *19*, 29–39. [CrossRef]
16. Seong, N.; Kim, J.; Choi, K. Analysis of Temperature and Relative Humidity Distribution According to Internal Airflow Changes in Underground Utility Tunnels Using CFD. *J. KIAEBS* **2018**, *12*, 245–256.
17. Yoon, D.; Seong, N.; Shin, D. A Study on Condensation Identification Through Internal Environment Measurement of Underground Utility Tunnels. *J. Korean Soc. Living Environ.* **2014**, *21*, 903–910. [CrossRef]
18. Peavy, B.A. Heating and Cooling of Air Flowing Through an Underground Tunnel. *J. Res. Natl. Bur. Stand. Sect. C* **1961**, *65*, 151–160. [CrossRef]
19. Li, W.; Wu, Y.; Fu, H.; Zhang, J. Long-Term Continuous In-Situ Monitoring of Tunnel Lining Surface Temperature in Cold Region and Its Application. *Int. J. Heat Technol.* **2015**, *33*, 39–44. [CrossRef]
20. Liu, J.; Aizawa, H.; Yoshino, H. CFD Prediction of Surface Condensation on Walls and Its Experimental Validation. *Build. Environ.* **2004**, *39*, 905–911. [CrossRef]
21. Jodat, A.; Moghiman, M.; Rad, E.Y. An Experimental Study of Ability of Similarity Theory to Predict Water Evaporation Rate for Different Convection Regimes. *Int. J. Multidiscip. Sci. Eng.* **2012**, *3*, 20–25.
22. Aldarabseh, S.M. Evaporation Rate from Free Water Surface. Master's Thesis, Western Michigan University, Kalamazoo, MI, USA, 2020.
23. Kim, Y.J. Causes and Countermeasures of Condensation in Road Tunnels. *J. Korean Tunn. Undergr. Space Assoc.* **2022**, *24*, 341–352.
24. Kim, H.G.; Lee, D.M.; Ryu, J.O. *Tunnel Fire Protection Engineering for Design of Tunnel Ventilation and Disaster Prevention Systems*; Donghwa Technology: Seoul, Republic of Korea, 2026; ISBN 978-89-425-9756-7.
25. Kibble, J.D. Some notes on mining diesels. *Mining Technology*, October 1978; pp. 393–400.
26. Launder, B.E.; Spalding, D.B. The Numerical Computation of Turbulent Flows. *Comput. Methods Appl. Mech. Eng.* **1974**, *3*, 269–289. [CrossRef]

27. Patankar, S.V. *Numerical Heat Transfer and Fluid Flow*; Hemisphere Publishing: Washington, DC, USA, 1980.
28. Wolf Dynamics. *Turbulence Modeling in OpenFOAM®: Guided Tutorials; Online Training–Advanced Session 2021*; Wolf Dynamics: Genoa, Italy, 2021; pp. 12–13.

https://doi.org/10.3390/infrastructures11060209